Journal of Membrane Science & Research

journal homepage: www.msrjournal.com

Research Paper

Composite Vanadium-Iron Metal Membrane for Hydrogen Recovery in Ammonia Production Unit

Ritu Parashar [1,2], Bipin Chandra Nailwal [2], Nitesh Goswami [2,*], Raja Kishora Lenka [3], Sourav Sarkar [4], Amit Kumar Singha [2], Krishna Kumar Singh [1,4], Asis Kumar Adak [2], Soumitra Kar [1,2], Suresh Chandra Parida [1,5], Sulekha Mukhopadhyay [1,4]

[1] *Homi Bhabha National Institute, Anushaktinagar, Mumbai - 400094*
[2] *Desalination & Membrane Technology Division, Bhabha Atomic Research Centre, Trombay, Mumbai - 400085*
[3] *Powder Metallurgy Division, Materials Group, Bhabha Atomic Research Centre, Vashi Complex, Navi Mumbai - 400705*
[4] *Chemical Engineering Division, Bhabha Atomic Research Centre, Trombay, Mumbai - 400085*
[5] *Product Development Division, Bhabha Atomic Research Centre, Trombay, Mumbai – 400085*

Article info

Received 2022-02-22
Revised 2022-10-19
Accepted 2022-10-20
Available online 2022-10-20

Keywords

Vanadium-Iron (V-Fe) metal membrane
Hydrogen-Helium separation
Computational Fluid Dynamics (CFD)
Helium recovery
Natural gas
Ammonia synthesis

Highlights

- Composite clay alumina support fabricated with optimized parameters and characterized
- Vanadium Iron alloy composite metal membrane fabricated and characterized
- Performance evaluation of metal membrane permeator for H_2-He separation
- Modeling and simulations of scaled-up metal membrane permeator for parametric optimization

Graphical abstract

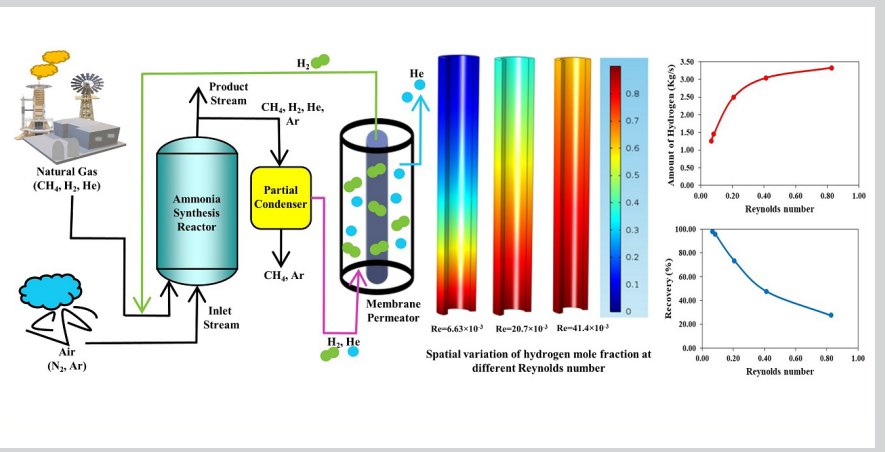

Abstract

Hydrogen separation from purge gas of ammonia production unit is an important step for maintaining the desired composition of gas in ammonia synthesis reactor, with an overall objective of helium concentration. Metal membranes, owing to high selectivity (typically >10,000) for hydrogen, are potential candidates for separation of hydrogen from un-reacted hydrogen-helium mixture. In this work, we report for the first time, fabrication, characterization and testing of composite Vanadium-Iron (V: 95 mol% - Fe: 5 mol%) metal membrane for separation of hydrogen - helium gas mixture, and CFD simulation of V-Fe membrane permeator. The clay-alumina support tubes were fabricated with optimized composition of 8% clay and 92% alumina, sintered at 1400 ºC. At optimized composition, average pore size of support was found to be 1.5 µm with a porosity of ~ 37%. The hydrogen permeance of V-Fe membrane was found to be ~ 300 GPU with no helium detected in the permeate. CFD simulation studies were carried out for single-tube (78.5 cm^2) as well as scaled-up membrane permeator having a total membrane area of 0.22 m^2. Optimized set of parameters to achieve a hydrogen recovery of >95% (flow rate: 7.17 kg/s) was found to be: Reynolds number: 8.28×10^{-3}, Feed-side pressure: 5 bar, Annular space for feed flow: 28.98 mm. The study provides valuable inputs for design and development of commercial metal membrane permeator for separation of hydrogen from the helium present in purge gas of ammonia production unit.

* Corresponding author: niteshg@barc.gov.in (N. Goswami)

DOI: 10.22079/JMSR.2022.549300.1534

1. Introduction

In the ammonia manufacturing process, steam methane reforming of natural gas is carried out to produce hydrogen as a feedstock. Natural gas consists mainly of methane, light hydrocarbons, helium, and nitrogen. As the helium present in natural gas doesn't participate in the ammonia synthesis reaction, it accumulates in the reactor [1].

Fig. 1 shows the flowsheet of helium recovery from purge gas of the ammonia synthesis reactor. This unreacted gas goes to a partial condenser where methane and argon are separated from the unreacted stream and recycled back to the ammonia reactor [1]. In order to avoid the increase in the partial pressure of helium in the ammonia reactor, helium needs to be recovered from the hydrogen-rich stream. At the same time, this stream can act as a source of helium as it has a helium concentration of ~ 3%, which is quite high. After the separation of hydrogen and helium, the recovered hydrogen is recycled back to the ammonia synthesis reactor. The separation of hydrogen from helium is difficult due to their similar size [helium (2.60 Å) and hydrogen (2.89 Å)] and low boiling points [2]. A commonly used technique for the separation of helium is cryogenic distillation which is costly and energy intensive. Natural gas fields are mostly under high pressure to make exploitation and distribution cost-effective, and a high-pressure stream is more suited for membrane and pressure swing adsorption in comparison to cryogenic distillation [3,4].

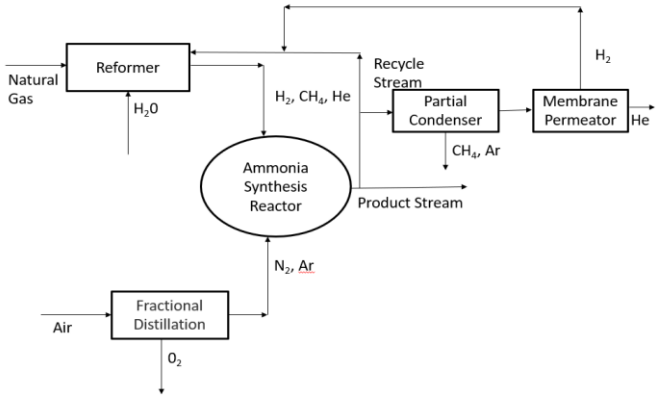

Fig. 1. Flow sheet of ammonia production unit.

Separation of hydrogen from helium can be done using membranes, as they offer the benefits of high selectivity along with ease of operation and scale-up. Polymeric, metallic, ceramic, and porous carbon membranes are used in gas separation applications in general [5–10], and for hydrogen separation in particular [11–14]. Recovery of helium from the gas mixture using a membrane-based process would be an energy-efficient method. Both polymeric and inorganic membranes have been reported in the literature for helium separation from natural gas [15]. Among the polymeric membranes, there is a need for improvement in the selectivity of helium with respect to other gases in order to achieve the desired purification and recovery [16]. Wei et al. [17] have carried out hydrogen and helium separation from Ne, Ar, N_2, CO, CO_2, H_2S, H_2O, and CH_4 gas mixture using porous graphene membranes. In order to separate hydrogen isotope (H_2 and D_2) from helium (in nuclear fusion reactors), Antunes et al. used MFI-ZSM-5 zeolite-type membranes (Porous inorganic membranes) [18]. The reported selectivity of H_2/He and D_2/He was only marginally greater than Knudsen diffusion selectivity. Metal membranes are unique candidates for hydrogen separation as they have infinite selectivity towards hydrogen [19–23]. It is also reported by Liguori et al. [24] that metal membranes exhibit superior hydrogen selectivity and permeability at the same pressure gradient that can range from 1000 to 10,000 times higher than polymeric membranes. Hydrogen separation through a metal membrane takes place through the solution diffusion mechanism. Most of the reported works carried out focus on palladium (Pd) – based metal membranes for hydrogen separation [25–31]. However, Pd involves challenges like moderate permeation flux, the higher tendency of hydrogen embrittlement, and higher cost [32,33].

As an alternative to Pd metal, several affordable metals like V and their alloys, have been investigated by researchers [27,34,35]. Low cost and high hydrogen permeability [34] (Pd: ~ $1x10^{-8}$ and V: 1.9 x 10^{-7} $mol.m^{-1}.s^{-1}.Pa^{-0.5}$ at 500 ˚C) make V-based membranes a more attractive alternative for Pd-based membranes [34–37]. One of the biggest problems with V metal membranes is hydrogen embrittlement since V typically generates vanadium hydride at room temperature and high hydrogen concentrations. V has a BCC structure, but vanadium monohydride (VH) has a body-centered tetragonal structure, while vanadium dihydride VH_2 has an FCC structure. The material fractures as a result of the phase change of V with hydride production. Operating the membrane above the metal's critical temperature or alloying it with a suitable metal increases its resistance to hydrogen embrittlement. For the V membrane, ductile–to–brittle transition occurs at a hydrogen concentration in the order of 0.2 ~ 0.25 (H/M). Alloying Fe in V reduces the H/M ratio in alloy and hence reduces the tendency of hydrogen embrittlement [38]. However, V and its alloys have a high tendency of being oxidized and hence they are usually coated with Pd or Pd-based alloys [39]. However, the coating of Pd and its alloys over V restricts the operating temperature due to interdiffusion among the metals [40]. One of the simplest methods to avoid this situation is to operate the system at a lower temperature. V has one of the highest hydrogen diffusion coefficients with low activation energy for hydrogen diffusion [41]. Alloying Fe with V reduces the solubility of hydrogen in alloy [42,43]. Furthermore, it has been noted that the disorganized BCC V-Fe alloy's hydrogen diffusivity (D) is relatively high and even exceeds that of pure V [40,42]. The atomic hydrogen flux of V-10 mol% Fe alloy membrane is reported as 55 × 10^{-6} $mol.m^{-1}.s^{-1}$ (almost 5 times Pd- 23% Ag alloy) [40]. Alimov et al. [43] developed a V alloy membrane and reported flux of membranes was found in this order: V-5.6Fe-0.8Pd > V-4.3Pd > V-10Fe > V-8.9Pd > V-10.6Fe-0.9Pd > V-13.3Pd (alloying composition in atom%).

To the best of our knowledge, the application of metal membranes in recycle stream of the ammonia production process has not been envisaged. At the same time, the literature reported on V-Fe alloy membranes does not have this composition (95 mol % V, 5 mol% Fe). CFD modeling and simulations of V-Fe membrane for hydrogen-helium separation have also not been reported yet in the literature and the same has been carried out for the first time by the authors. In this work, we report the development of a V-Fe (95-5 mol%) metal membrane by coating V-Fe alloy over composite ceramic support using DC magnetron sputtering. Characterization and gas permeation studies of composite V-Fe membranes were also carried out. CFD simulation studies were carried out for the entire composition range of hydrogen-helium mixture (10-90% of He in H_2) for single-tube as well as scaled-up membrane permeator. Modeling and simulation studies, in addition, aided in analyzing the effects of various operating conditions and geometric parameters on the performance of membrane permeator.

2. Experimental methods & computational approach

2.1 Development of asymmetric ceramic support

Commercial-grade alumina and clay were used as raw materials. Green clay-alumina tubes were prepared by extrusion of clay-alumina slurry. The clay-alumina support tubes of composition 8% clay (47% SiO_2, 38% Al_2O_3, rest Fe_2O_3, TiO_2, and low ignition compounds), 92% alumina (tube 1), and 15% clay,85% alumina with MgO as 0.5% of total weight (tube 2), were sintered as per sintering profiles shown in Table S1 of Supplementary Information. Characterization of the clay-alumina tube was carried out using a scanning electron microscope (SEM, Zeiss EVO 18) and mercury (Hg) porosimeter (PASCAL- 440).

The pore size of the support tube was reduced by coating the intermediate alumina layer over clay-alumina base support. Alumina (particle size: ~190 nm) coating on base clay-alumina support tubes was done by dip coating method as per the procedure described in our earlier work [44] and provided in the Supplementary Information.

2.2 Fabrication of V-Fe metal membrane by DC magnetron sputtering

V-Fe (95-5 mol %) alloy target of 99.95% purity was used for sputter coating. The thin film of V-Fe metal was coated over asymmetric ceramic support by the DC magnetron sputter deposition technique (layout of the machine provided in Fig. S1 of Supplementary Information). Before deposition, a base vacuum of 5 x 10^{-6} torr was maintained in the sputtering chamber. The deposition is carried out for 3 hours at a temperature of 500 ˚C. After deposition, the membrane with an approximate coating thickness of ~ 4 µm was vacuum annealed at 1000 ˚C for 2 h to obtain defect-free coating. A thin layer (100 nm) of Pd (75 wt%) - Ag (25 wt%) was coated on the V-Fe alloy membrane using the DC magnetron sputtering method.

2.3 Flux and selectivity studies of V-Fe metal membrane

Fig. 2 consists of the membrane permeator, V-Fe membrane, end connectors, and graphite ferrules. Sealing of membrane with end connector is carried out using graphite ferrule. ID and OD of graphite ferrule are 12 and 20 mm and a tapered angle of 57˚ is maintained. The dimension of the membrane

is 12 mm OD, 8 mm ID, and 250 mm in length. Feed is passed through the annular space of the membrane permeator and the product is collected through the tube. Helium leak testing of the membrane permeator was carried out, and a leak rate of 10^{-4} mbar.liter/s was found.

Gas permeation testing of the V-Fe coated composite membrane was carried out at room temperature to ensure that the membrane is defect-free, using an in-house developed gas permeation test setup (Fig. S2 of Supplementary Information). The gas permeation studies were carried out in semi-batch mode (reject and feed lines were closed once the required pressure was achieved, and the product line was kept open). Three different feed gas mixtures were used (pure He, pure H_2, and a mixture of 90% H_2-10% He) for permeation testing.

Sievert's law (Equation 1) is used to calculate the Permeance (ϕ) of a V-Fe metal membrane [45]:

$$J = \phi \times \Delta P^n \quad (1)$$

where J is the flux of membrane in mol.m^{-2}.s^{-1}, ϕ is permeance in mol.m^{-2}.s^{-1}Pa^{-n}, ΔP is trans-membrane pressure in Pa, n is an exponent & a function of membrane thickness [30,46].

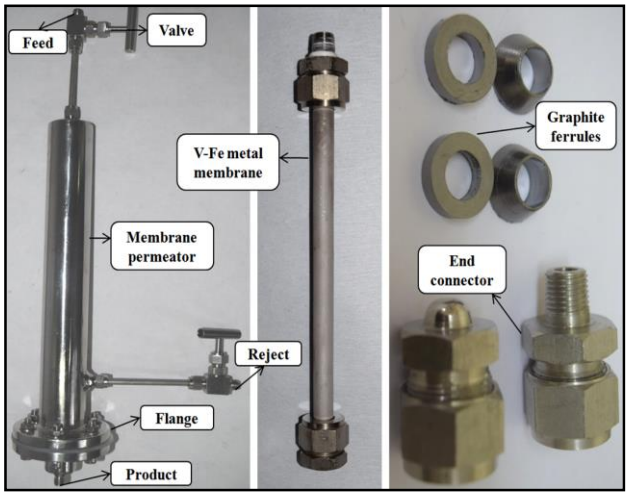

Fig. 2. Membrane permeator showing the individual components (metal membrane, end connectors, and graphite ferrules).

2.4 CFD simulations

CFD modeling was carried out using COMSOL Multiphysics. Momentum, energy, and species transport mechanism (physics) were considered in the CFD simulations. To model momentum transport, the Navier-Stokes equation was used. For energy transport, both convective and conductive transport equations were solved. For species transport, the Maxwell-Stefan diffusion and convection equation was considered. The governing equations for momentum, energy and species transport, physical properties, assumptions, and boundary conditions are provided in Section S.2 of Supplementary Information. Grid independence tests were also carried out for both single-tube and scaled-up membrane permeators (Fig. S7 (a) and (b) of Supplementary Information). The CFD model was validated by comparing the velocity profile predicted by the model for the case of zero hydrogen flux with the analytical velocity profile (Fig. S8 of Supplementary Information). The hydrogen flux through the membrane wall has been defined by Equation 2.

$$H_f = -Pe \times p \times x_{H_2} \times M_{H_2} \quad (2)$$

where H_f is the permeation flux of hydrogen in kg/m^2.s, Pe is the hydrogen permeance in mol.m^{-2}.s^{-1}Pa^{-1}, p is the total pressure in Pa, x_{H2} is the mole fraction of hydrogen and M_{H2} is the molecular mass of hydrogen. The recovery of hydrogen was calculated using Equation 3.

$$Recovery = \frac{Amount\ of\ hydrogen\ passing\ through\ the\ membrane}{Amount\ of\ hydrogen\ entering\ through\ the\ membrane\ permeator} \quad (3)$$

3. Results and discussion

3.1 Effect of composition on the fabrication of clay-alumina base support

The morphology and pore size of the tubes were analyzed through SEM and mercury porosimeter. Fig. 3 (a) and (b) show the SEM images of tubes 1 and 2, respectively. As evident from the images, tube-1 has got better connectivity of pores, whereas tube-2 was found to have patches of densified zones with reduced interconnectivity of pores. The porosimeter analysis showed that tube-1 has most of the pores in the range of 1.0 to 2.0 µm with ~ 37% porosity, while tube-2 has most of the pores varying from 0.5 to 1.0 µm with ~ 16% porosity. Since both the tubes have maximum pore sizes above 1 µm, porosity is the determining factor in the selection of the support tube. As MgO is added in tube-2, it reacts with SiO_2 (which is present in clay) to form $MgSiO_3$ which results in small patches as seen in SEM images, owing to liquid phase sintering. This liquid phase fills the pores at several locations and upon cooling, this liquid again gets solidified, resulting in patch formation. This results in a decrease in the permeability of the sample, though the largest pore size and pore size distribution remain nearly the same. To avoid the pore closure in the support, the use of MgO was thus avoided. Clay is added to alumina to reduce the sintering temperature. As clay is a low melting compound, it results in the reduction of sintering temperature and acts as a sintering aid. However, a lower concentration of clay (8%) was preferred to avoid the impurities associated with clay in the tube. Owing to the higher porosity of tube-1, which is the main requirement of the support to be used for separation applications, the composition used for the fabrication of tube-1 was taken to be the optimum for further studies.

3.2 Effect of sintering temperature on the fabrication of clay-alumina base support

Tubes of clay-alumina mixture in the ratio of 92:8 were sintered at 1300, 1400, and 1500 ˚C to study the effect of temperature on pore size and porosity of the membrane. Table 1 shows the comparison of tubes sintered at different temperatures. Hg porosimetry results show that the tubes sintered at 1300, 1400, and 1500 ˚C have a maximum pore size in the range of 1 to 2 µm. With the increase in sintering temperature, total cumulative volume, and porosity decrease. All these findings indicate that with an increase in sintering temperature, higher densification takes place. Interestingly, the tubes sintered at 1300 ˚C were found to be fragile and brittle in nature. Thus, the support tubes were sintered at 1400 ˚C.

Table 1
Comparison of clay-alumina tubes sintered at different temperatures.

Parameter	Sintering temperature		
	1300˚C	1400˚C	1500˚C
Total cumulative volume (mm^3/g)	199.627	182.353	160.77
Total specific surface area (m^2/g)	3.479	1.15	1.504
Average pore diameter (µm)	1.374	1.531	1.388
Total porosity (%)	40.832	37.639	35.104

3.3 Characterization of alumina-coated clay-alumina tube

The morphology and pore size of the alumina-coated clay-alumina tube were analyzed through SEM. SEM images of the bare and coated tubes are shown in Fig. 4 (a) and (b), respectively. As evident from SEM images, the gamma alumina coating has reduced the porosity and pore size of the top layer significantly. The coating thickness of alumina varies from 3 to 6 µm, while surface analysis showed that after gamma alumina coating the pore size of the surface was reduced to ~ 200 nm (pores size are estimated by ImageJ software).

3.4 Characterization of V-Fe metal membrane

3.4.1 Morphology analysis using a scanning electron microscope (SEM)

Fig. 5 (a) shows the surface morphology of the V-Fe metal membrane as analyzed through SEM. As clearly evident from the morphology, the membrane has a dense V-Fe layer with no visible pores. Fig. 5 (b) shows the SEM cross-section image of the V-Fe metal membrane which shows a coating thickness of the active layer is ~ 4 µm.

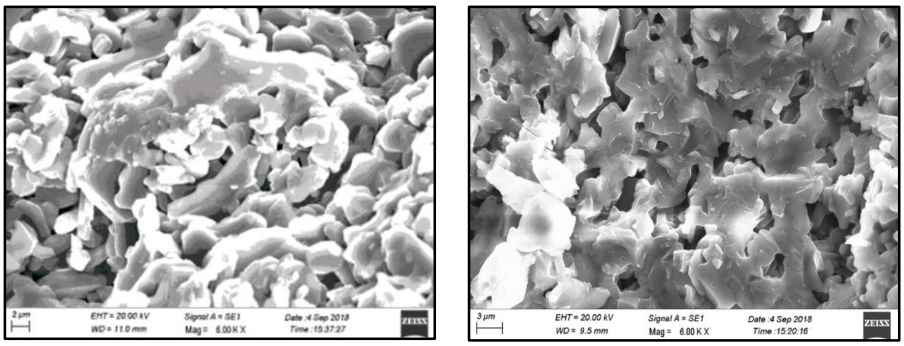

(a) SEM image of tube-1. (b) SEM image of tube-2.

Fig. 3. SEM images of tubes1 and 2.

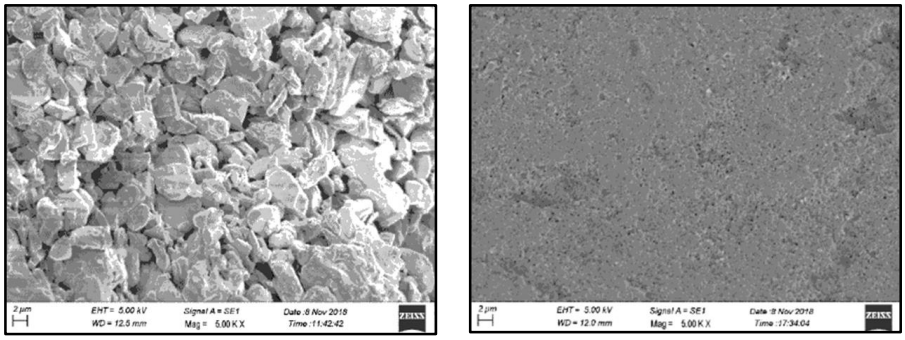

(a) SEM image of the surface of support tube 1. (b) SEM image of the surface of gamma alumina coated tube 1 with optimized slurry.

Fig. 4. SEM image of support tube before and after gamma coating.

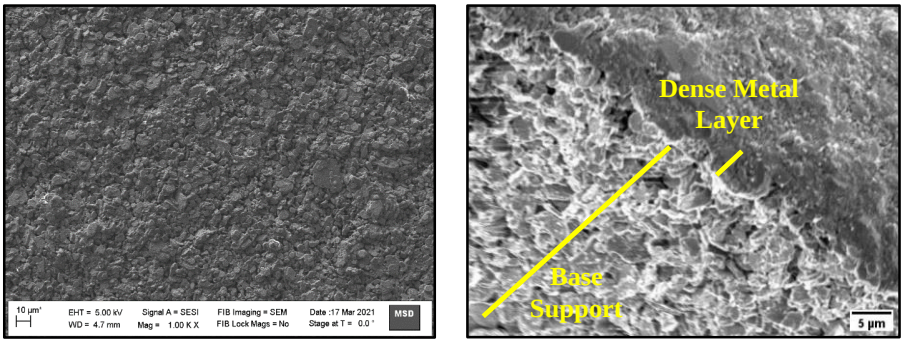

(a) Surface morphology of V-Fe metal membrane. (b) Cross-sectional morphology of V-Fe membrane.

Fig. 5. Morphology of V-Fe metal membrane with cross-section image.

3.4.2 Energy-dispersive spectroscopy (EDS)

The EDS mapping image (Fig. 6) of the V-Fe metal membrane is taken at 20 keV electron beam energy. The results clearly show the presence of V, Fe, Al, Si, and O. The presence of Al, Si, and O revealed in the EDS image is due to alumina. Oxygen traces are also seen, which are mostly found in the locations having the presence of aluminum that is because of the Al_2O_3 support. The presence of Si is also observed in support that comes from the clay used as sintering aids. The constituents of support are observed in EDS mapping, as the typical penetration depth is ~ 5 µm.

3.5 Gas permeation studies of V-Fe metal membrane

The in-house synthesized composite alumina tubes and V-Fe metal membranes are shown in Fig. S3 and Fig. S4 (Supplementary Information). Table 2 shows the results of gas permeation studies carried out. It can be seen that with pure helium, no flux was obtained on the permeate side which indicates the defect-free nature of the metal membrane. With pure hydrogen, a flux of ~ 18 LMH was obtained. Gas permeation studies were carried out with different gas compositions, considering the possibility that PSA/Cryogenic unit might not be used to remove inert gases like argon and nitrogen from the recycle stream in the ammonia synthesis process. It is observed that with a decrease in the concentration of hydrogen in feed, the flux of hydrogen through the membrane decreases, which is due to a reduction in the driving force (partial pressure of hydrogen). At the same time, higher flux has been observed at high temperatures, which is due to an increase in the rate of diffusion of hydrogen atoms at a higher temperature. [35,38]. In all the compositions, hydrogen purity of> 99.9% was obtained.

3.6 Modelling and simulation studies

The effect of various process and geometry parameters, like feed composition, Reynolds number, membrane length, and membrane permeator (housing) diameter on the recovery of hydrogen from a hydrogen-helium mixture has been studied using CFD simulation. It is assumed that other inert gases have been removed from the feed stream by using cryogenic/PSA to get higher hydrogen partial pressure in the permeator feed. At the same time, the effect of scaling up of membrane from 78.5 cm^2 to 0.22 m^2 has been also studied.

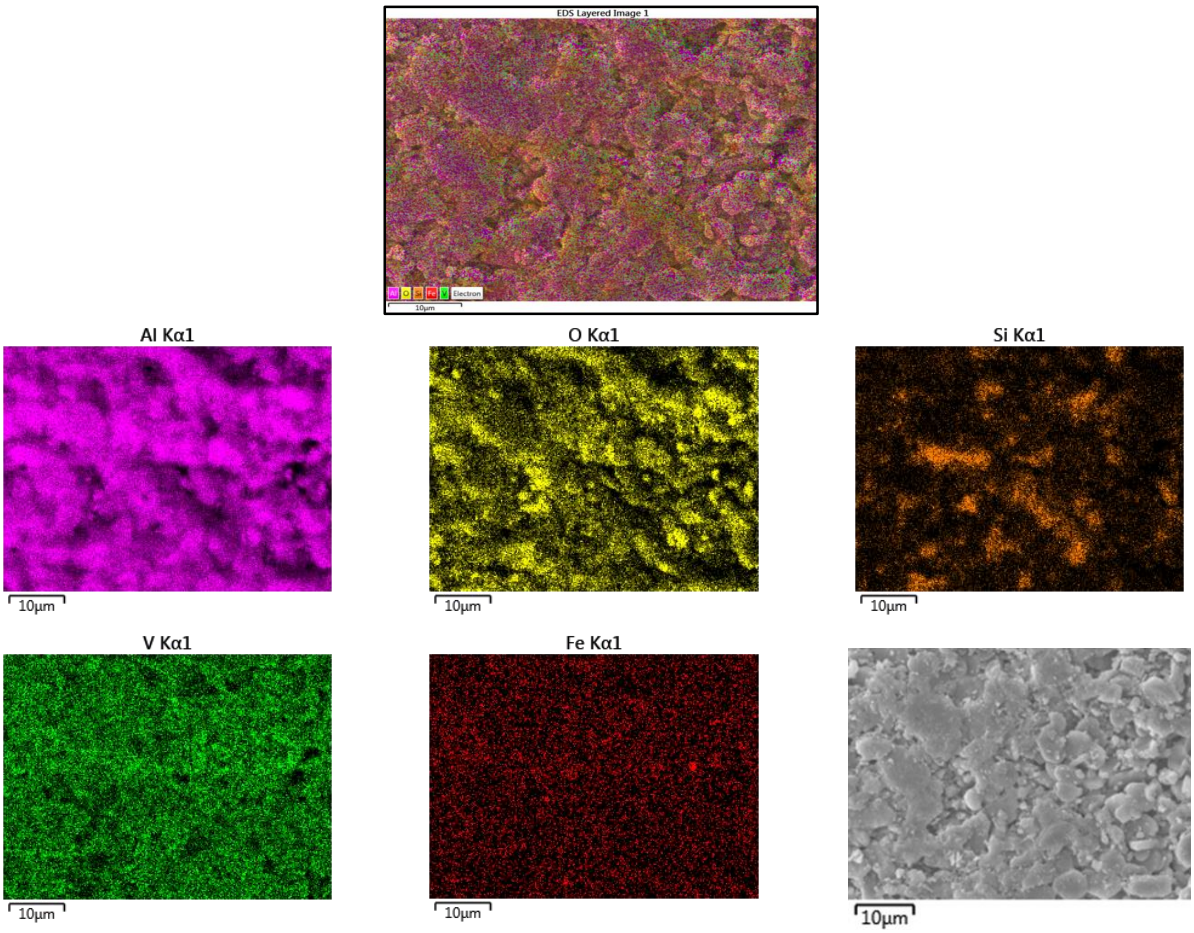

Fig. 6. EDS mapping images of V-Fe metal membrane.

Table 2
Results of gas permeation studies carried out at room temperature and 450 ˚C.

Feed composition	Pressure (bar)	Temperature (˚C)	Flux (LMH)	Remarks
He: 100%	1.0	RT	0	No, He detected
H_2: 100%	1.0	RT	18 ± 2	100% H_2 in permeate
H_2: 90%, He: 10%	1.0	RT	16 ± 1	H_2 purity: > 99.9%
H_2: 90%, He: 2%, Ar: 2%, N_2: 6%	1.0	RT	17 ± 2	H_2 purity: > 99.9%
H_2: 85%, He: 1%, Ar: 1%, N_2: 13%	1.0	RT	12 ± 2	H_2 purity: > 99.9%
H_2: 80%, He: 0.1%, Ar: 1%, N_2: 13.9%	1.0	RT	8 ± 1	H_2 purity: > 99.9%
H_2: 100%	0.1	200	34 ± 2	100% H_2 in permeate
H_2: 100%	0.5	200	142 ± 5	100% H_2 in permeate
H_2: 100%	0.1	450	71 ± 5	100% H_2 in permeate
H_2: 100%	0.5	450	352 ± 8	100% H_2 in permeate
H_2: 100%	1	450	670 ± 12	100% H_2 in permeate

3.6.1 Effect of Reynolds number on hydrogen mole fraction profile

The effect of Reynolds number (for a constant flow area) on the axial profiles of mole fraction of hydrogen at a radius of 6.035 mm is shown in Fig. 7. It is observed that with an increase in Reynolds number from 1.18×10^{-3} to 11.8×10^{-3}, the mole fraction of hydrogen at the outlet increases from 0.0579 to 0.6594. With the increase in Reynolds number, residence time in the membrane permeator reduces leading to a reduction in hydrogen permeation flux. As the lower amount of hydrogen permeates through the membrane, the higher mole fraction of hydrogen is observed at the outlet of the permeator. The axial profiles showed that hydrogen mole fraction along the length decreases initially at a higher rate and then the rate decreases. This is because the partial pressure of hydrogen across the membrane reduces with a reduction in the mole fraction of hydrogen (Equation 2). Initially the reduction in mole fraction with length is linear and then the mole fraction reduces non-linearly. At a higher Reynolds number, the linear decrease continues till the exit of the permeator. So, it would be preferable to operate the metal membrane permeator at a low Reynolds number for better separation. So, Reynolds number 1.18×10^{-3} is considered optimum. However, it will be at the cost of lower throughput.

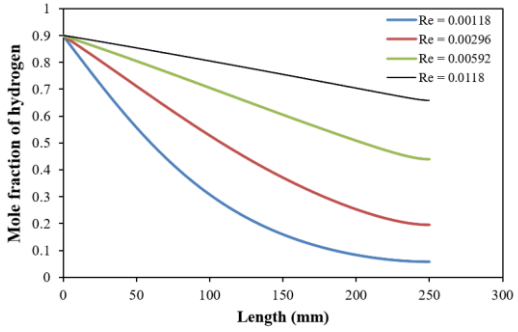

Fig. 7. Variation of hydrogen mole fraction along the length for different Reynolds numbers (L=250 mm, D_h=14.14 mm, T_f=600 K, T_w=700 K, P= 1 bar, x_{H2}= 0.9).

3.6.2 Effect of Reynolds number on hydrogen flux through the membrane

Fig. 8 shows the amount of hydrogen obtained from the permeator for different Reynolds numbers as predicted by the CFD model. It is observed that for a constant outlet pressure (101325 Pa), with an increase in Reynolds number, the amount of hydrogen increases. The amount of hydrogen increases from 0.00446 to 0.0112 Kg/s with an increase in Reynolds number from 1.18×10^{-3} to 11.8×10^{-3}. With an increase in Reynolds number from 1.18×10^{-3} to 11.8×10^{-3}, the residence time for permeation reduces leading to an increase in the average mole fraction of hydrogen from 0.3117 to 0.7792. It is also observed that the amount of hydrogen increases steeply at a lower Reynolds number (till 0.00592), but at a higher Reynolds number the increase is not significant. This is because, with an increase in Reynolds number, the average mole fraction of hydrogen inside the membrane permeator tends to become constant inching closer to the feed mole fraction. Thus, with the continued increase in Reynolds number, the total permeation flux also tends to become constant. Fig. 9 gives the variation of hydrogen flux along the length of the membrane for different Reynolds numbers.

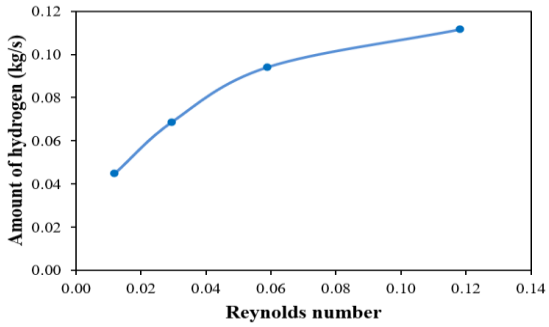

Fig. 8. Variation of the amount of hydrogen with Reynolds number (L=250 mm, D_h=14.14 mm, T_f = 600 K, T_w = 700 K, P = 1 bar, x_{H2}= 0.9).

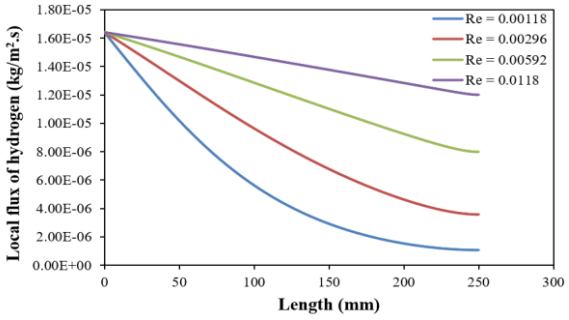

Fig. 9. Local permeation flux of hydrogen along the length of membrane for different Reynolds numbers (L=250 mm, D_h=14.14 mm, T_f=600 K, T_w= 700 K, P = 1bar).

3.6.3 Effect of Reynolds number on recovery of hydrogen

The variation of recovery of hydrogen with Reynolds number, as predicted by the CFD model, is shown in Fig. 10. It can be observed that recovery of hydrogen decreases with an increase in Reynolds number. With the increase in Reynolds number, the permeation flux and hydrogen inlet flux increase as shown in Fig. 11. However, at a higher Reynolds number, the increase in permeation flux is not able to balance the increase in the inlet flux of hydrogen. This causes recovery to reduce. Hence, there is an optimum Reynolds number ($Re=1.18 \times 10^{-3}$) for maximum recovery of hydrogen. Fig. 12 shows the spatial variation of the mole fraction of hydrogen in the metal membrane permeator for different Reynolds numbers. It can be observed that a lower Reynolds number allows more hydrogen removal. As Reynolds number is increased, a higher mole fraction of hydrogen persists up to a longer length of the permeator.

3.6.4 Effect of hydrogen mole fraction in the feed on axial mole fraction profile

Fig. 13 shows the variation of hydrogen mole fraction along the length for a feed having different hydrogen mole fractions. It is observed that at lower hydrogen concentration at the inlet, the rate of decrease of mole fraction along the permeator length decreases. This is because a lower feed mole fraction results in lower hydrogen partial pressure leading to a gradual decrease in the hydrogen mole fraction along the length.

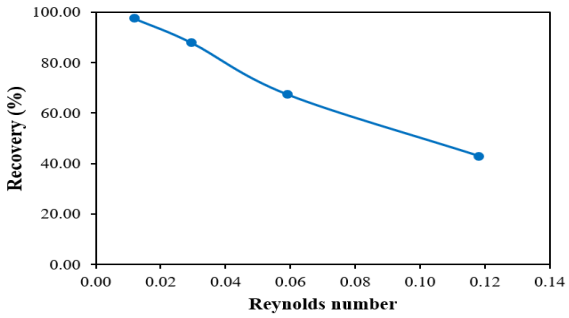

Fig. 10. Variation of hydrogen recovery with Reynolds number (L=250 mm, D_h=14.14 mm, T_f = 600 K, T_w = 700 K, P = 1 bar, x_{H2}= 0.9).

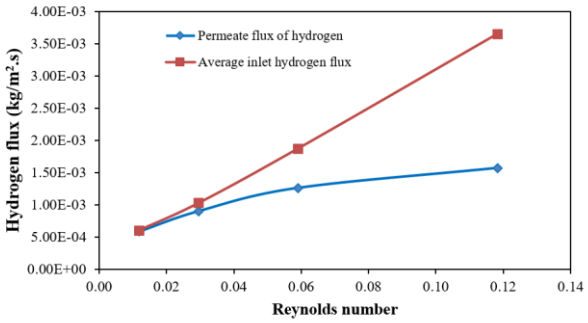

Fig. 11. Variation of average inlet flux and permeate flux of hydrogen with Reynolds number (L=250 mm, D_h=14.14 mm, T_f = 600 K, T_w = 700 K, P = 1 bar, x_{H2}= 0.9).

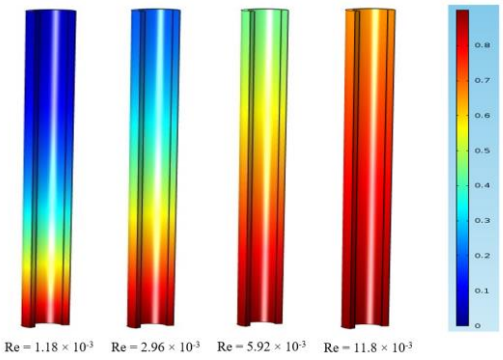

Fig. 12. Spatial variation of hydrogen mole fraction inside the membrane permeator at different Reynolds numbers (L=250 mm, D_h= 14.14 mm, T_f = 600 K, T_w = 700 K, P = 1 bar, x_{H2}= 0.9).

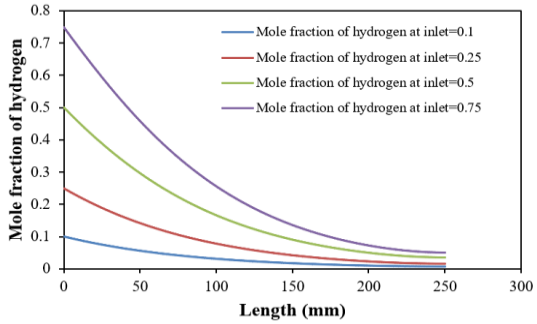

Fig. 13. Axial profiles of hydrogen mole fraction for different inlet hydrogen mole fractions (L=250 mm, D_h=14.14 mm, Re = 1.18×10^{-3}, T_f = 600K, T_w = 700K, P = 1 bar).

3.6.5 Effect of hydrogen mole fraction in feed on flux and recovery

Fig. 14 shows the recovery of hydrogen for different mole fractions of hydrogen in the feed, respectively, as obtained from the CFD model. It can be observed that recovery of hydrogen increases with a mole fraction of hydrogen (Equation 2). However, the rate of change of recovery is higher at a higher mole fraction because the length of the membrane exposed to a higher mole fraction of hydrogen increases, leading to an increase in overall flux and recovery.

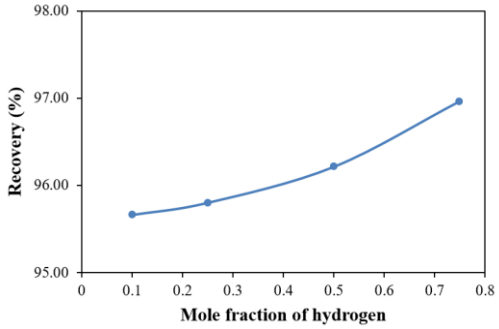

Fig. 14. Variation of recovery of hydrogen with inlet mole fraction of hydrogen (L=250 mm, D_h=14.14 mm, Re = 1.18 × 10^{-3}, T_f = 600 K, T_w = 700 K, P = 1 bar).

3.6.6 Effect of length of membrane permeator on hydrogen recovery

Fig. 15 shows the recovery of hydrogen for different lengths of membrane permeator for constant feed velocity (0.1 m/s). It is observed that the recovery of hydrogen increases from ~ 42.94 to 87.9 % with an increase in permeator length from 250 to 850 mm for a permeator housing diameter of 14.14 mm. This is because with an increase in the length of the membrane, the residence time of gas inside the reactor increases which results in increased hydrogen removal. It is observed that the slope of the curve reduces with the length. This is because the mole fraction of hydrogen decreases along the length, and so does the permeation flux of hydrogen.

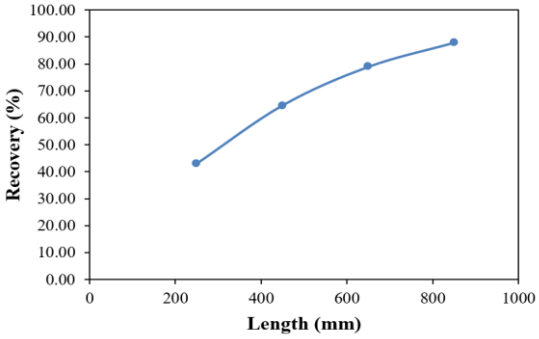

Fig. 15. Variation of recovery of hydrogen with a length of permeator (D_h=14.14 mm, u_0=0.1 m/s, T_f =600 K, T_w = 700 K and P= 1 bar, x_{H2}= 0.9).

3.6.7 Effect of the diameter of membrane permeator on hydrogen recovery

Fig. 16 shows the recovery of hydrogen for different diameters of membrane permeator fora constant feed velocity of 0.01 m/s. It is observed that the recovery of hydrogen decreases from 97.64 to 77.62 % with an increase in membrane housing diameter from 14.14 to 20.35 mm at a permeator length of 250 mm. This is because, with an increase in diameter, the flux of hydrogen entering into the permeator (average inlet flux) increases, whereas the permeation flux is not increasing sufficiently to balance inlet flux. As our targeted recovery is 95%, the optimum diameter of the housing is 15.18 mm. It is observed that flux through the membrane permeator has increased by 20% with an increase in housing diameter from 14.14 to 15.18 mm.

The CFD simulation studies indicate that beyond a certain permeator length, less utilization of the membrane takes place due to lower driving force (partial pressure difference) for hydrogen permeation. At the same time, a lower diameter is a better option to achieve higher recovery. Optimized parameters for a single tube membrane permeator operation (78.5 cm^2) to achieve a recovery of more than 95% for a feed having a hydrogen mole fraction of 0.9 are Reynolds number: 1.18× 10^{-3}, Pressure: 1 bar, Annular space for feed flow: 5.18 mm and membrane length of 250 mm with 10 mm diameter. At optimized conditions, the flow rate of hydrogen through the membrane was 5.27 × 10^{-2} kg/s.

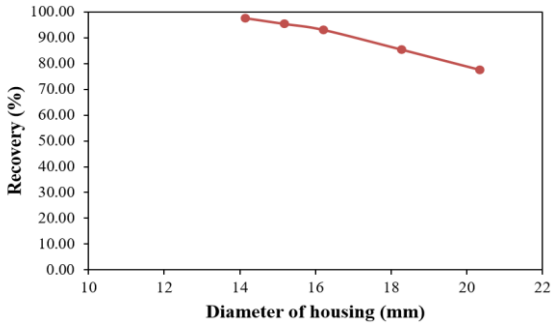

Fig. 16. Variation of recovery of hydrogen with a diameter of permeator (L=250 mm, u_o=0.01 m/s, T_f =600 K, T_w = 700 K and P= 1 bar, x_{H2}= 0.9).

3.7 CFD simulation studies for scaled-up membrane permeator

3.7.1 Effect of Reynolds number on hydrogen recovery

The variation of hydrogen recovery with Reynolds number for a scaled-up membrane permeator is shown in Fig. 17. It can be observed that a higher hydrogen recovery is achieved at a lower Reynolds number. The amount of hydrogen passing through the membrane increases with an increase in Reynolds number, as shown in Fig. 18. The amount of hydrogen increases from 1.25 to 3.33 kg/s with an increase in Reynolds number from 6.63 × 10^{-3} to 8.28 × 10^{-3}. The increase in permeation flux, however, is unable to counteract the increase in hydrogen inlet flux as the Reynolds number increases. This causes recovery to reduce. During scale-up, the recovery targeted is 95%, which is achieved for Reynolds number 8.28 × 10^{-3}. As shown in Fig. 19, the permeation flux and hydrogen inlet flux rise with an increase in Reynolds number. The spatial change of the mole percentage of hydrogen in the metal membrane permeator for various Reynolds numbers is shown in Fig. 20. Lower Reynolds numbers, as can be seen, permit higher hydrogen removal. Higher mole fractions of hydrogen persist along the permeator's whole length as the Reynolds number increases, and hence for better separation, it would be preferable to operate the metal membrane permeator at a low Reynolds number.

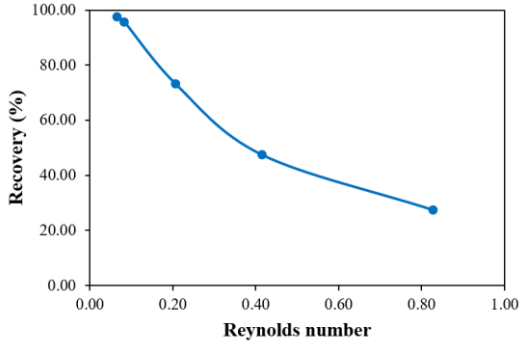

Fig. 17. Variation of percentage recovery of hydrogen with Reynolds number (L=1000 mm, D_h=98.98 mm, T_f = 600 K, T_w = 700 K, P = 1 bar, x_{H2}= 0.9).

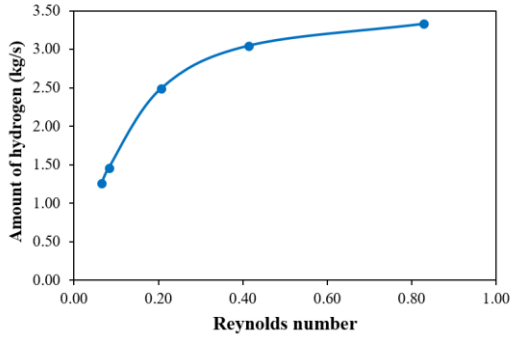

Fig. 18. Variation of the amount of hydrogen with Reynolds number (L=1000 mm, D_h=98.98 mm, T_f = 600 K, T_w = 700 K, P = 1 bar, x_{H2}= 0.9).

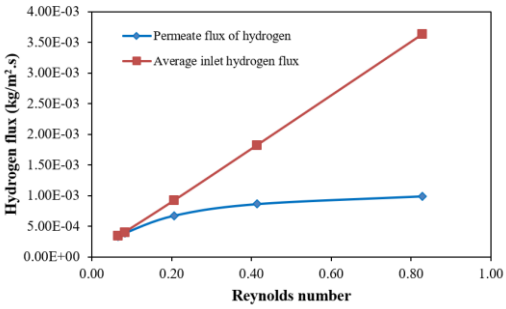

Fig. 19. Variation of average inlet flux and permeate flux of hydrogen with Reynolds number (L=1000 mm, D_h=98.98 mm, T_f = 600 K, T_w = 700 K, P = 1 bar, x_{H2}= 0.9).

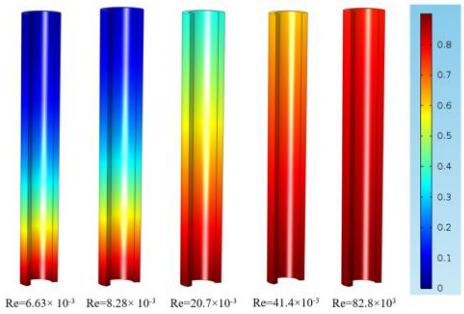

Fig. 20. Spatial variation of hydrogen mole fraction at different Reynolds numbers (L=1000 mm, D_h=98.98 mm, T_f = 600 K, T_w = 700 K, P = 1 bar, x_{H2}= 0.9).

3.7.2 Effect of pressure on the amount of hydrogen at the outlet

Fig. 21 shows the variation in the amount of hydrogen for different values of outlet pressure. It is observed that amount of hydrogen increases linearly from 1.25 to 7.17 kg/s as outlet pressure is increased from 1 to 5 bar. With the increase in outlet pressure, the pressure inside the permeator increases. Thus, the permeation flux of hydrogen, which is directly proportional to hydrogen partial pressure, also increases with an increase in outlet pressure (Equation 2). As base support is ceramic, pressure 5 bar is considered as optimum pressure due to the strength constraints of ceramic materials.

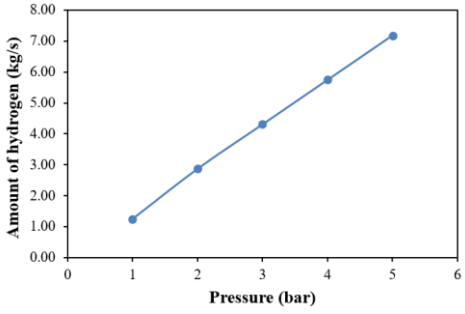

Fig. 21. Variation of the amount of hydrogen for different outlet pressure (L=1000 mm, D_h=98.98 mm, T_f = 600 K, T_w = 700 K, Re=0.00828, x_{H2}= 0.9).

3.7.3 Effect of the diameter of membrane permeator on hydrogen recovery

Fig. 22 shows the recovery of hydrogen for different diameters of membrane permeator for constant feed velocity 0.01 m/s. It is observed that the recovery of hydrogen decreases from 98.8 to 93.4 % with an increase in membrane housing diameter from 45.49 to 51.49 mm at a permeator length of 1000 mm. This is because an increase in diameter increases the flux of hydrogen entering the permeator while not affecting the permeation flux. Fig. 23 shows the amount of hydrogen for different diameters of membrane permeator for a constant feed velocity of 0.01 m/s. As the diameter increases, the amount of hydrogen is found to increase from 1.08 to 1.63 kg/s. This is because as the diameter of the membrane increases, the amount of inlet hydrogen increases, resulting in more hydrogen removal. For scale-up, the housing diameter of 49.49 mm is considered the optimum housing diameter because it allowed us to meet our objective of achieving more than 95% hydrogen recovery.

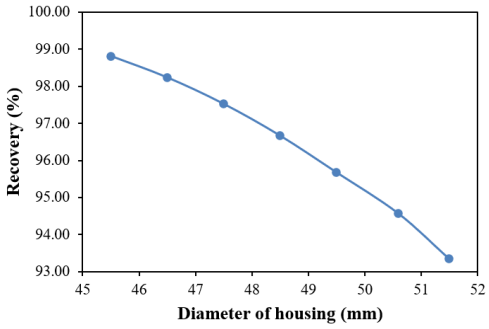

Fig. 22. Variation of recovery of hydrogen with a diameter of permeator (L=1000 mm, u_0=0.01 m/s, T_f =600 K, T_w = 700 K and P= 1 bar, x_{H2}= 0.9).

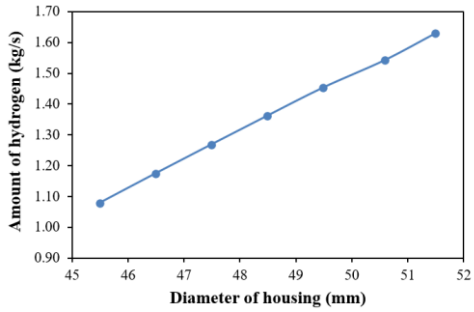

Fig. 23. Variation of the amount of hydrogen with a diameter of permeator (L=1000 mm, u_0=0.01 m/s, T_f=600 K, T_w = 700 K and P= 1 bar, x_{H2}= 0.9).

Optimized parameters for a scaled-up membrane permeator operation to achieve a recovery of more than 95% for a feed having a hydrogen mole fraction 0.9 are Reynolds number: 8.28 × 10^{-3}, Pressure: 5 bar, Annular space for feed flow: 28.98 mm and membrane length of 1000 mm with 70 mm diameter. At optimized conditions, the flow rate of hydrogen through the membrane was 7.17 kg/s which is ~ 135 times the flux of a single tube membrane permeator. The CFD simulation studies and the present findings are important in terms of designing a commercial membrane permeator for its successful operation.

4. Conclusions

Fabrication, characterization, and testing of composite Vanadium-Iron (V-Fe) metal membrane and membrane permeator for hydrogen-helium separation in the ammonia production unit were carried out. V-Fe (95-5 mol %) metal membrane was developed by depositing the alloy over composite ceramic support using DC magnetron sputtering. SEM, EDS, and mercury porosimetry analyses were carried out for the characterization of the membrane. Gas permeation studies of composite V-Fe membrane-based permeator were carried out for performance evaluation. Parametric studies using CFD simulations were carried out for analyzing the effects of various processes and geometry conditions on the flux and recovery of hydrogen. The optimum composition for the fabrication of a base clay-alumina support tube for the metal membrane was found to be clay (8%)-alumina (92%) and a sintering temperature of 1400˚C. The optimized membrane support has most of the pores in the range of 1.0 to 2.0 µm, with 37% porosity. Gamma alumina was coated over a composite support tube with a coating thickness of ~ 6 µm and a pore size of ~ 200 nm. The hydrogen gas permeance and selectivity for the V-Fe metal membrane were determined using gas permeation studies. The permeability of V-Fe for hydrogen was found to be ~ 300 GPU.

CFD simulations of the V-Fe membrane permeator for the separation of hydrogen from helium were carried out. The model was used to study the effect of Reynolds number, outlet pressure, and feed composition on the performance of the permeator. Optimized parameters for a single tube membrane permeator operation (78.5 cm^2) to achieve a recovery of more than 95% for a feed having a hydrogen mole fraction of 0.9 are Reynolds no: 1.18× 10^{-3}, pressure: 1 bar, annular space for feed flow: 5.18 mm and membrane length of 250 mm with 10 mm diameter. At optimized conditions, the flow rate of hydrogen through the membrane was found to be 5.27 × 10^{-2} kg/s. CFD simulation studies for scaled-up membrane permeator having a membrane area of 0.22 m^2 were also carried out. Optimized parameters for a scaled-up membrane permeator operation to achieve a recovery of more than 95% for a feed having a hydrogen mole fraction 0.9 are Reynold no: 8.28 × 10^{-3}, Pressure: 5 bar, Annular space

for feed flow: 28.98 mm and membrane length of 1000 mm with 70 mm diameter. At optimized conditions, the flow rate of hydrogen through the membrane was found to be 7.17 kg/s which is ~ 135 times the flux of a single tube membrane permeator. The study provides valuable inputs for the design and development of a commercial permeator for the separation of hydrogen from the helium purge gas of the ammonia production unit.

CRedit authorship contribution statement

R.Parashar: Data curation; Roles/Writing - original draft; Formal analysis.
B.C. Nailwal: Investigation; Methodology.
N. Goswami: Conceptualization; Validation; Visualization.
R.K. Lenka: Data curation.
S. Sarkar: Software; Validation.
A.K. Singha: Data curation.
S. Kar: Conceptualization; Writing - review & editing; Project administration.
K.K. Singh: Software; Validation.
A.K. Adak: Project administration; Resources; Funding acquisition.
S.C. Parida: Supervision; Writing - review & editing.
S. Mukhopadhyay: Supervision; Writing - review & editing.

Funding

This research is carried out as a part of R&D Project of Department of Atomic Energy, Government of India.

Declaration of Competing Interest

The authors declare that they have no known competing financial interests or personal relationships that could have appeared to influence the work reported in this paper.

Acknowledgment

We thank Mr. Vishal Singh, Materials Science Division, BARC for the SEM characterization of the membrane; Dr. A. Ghosh, Glass, and Advance Material Division, BARC for mercury porosimetry characterization; Mr. R. B. Bramhane and Mr. P. P. Surve from Desalination and Membrane Technology Division, BARC for their support in membrane fabrication and testing.

References

[1] A.A. Haslam, Treatment of ammonia synthesis purge gas, (1977). https://patentimages.storage.googleapis.com/a4/01/47/2517acdc7f085a/US4058589.pdf
[2] M.T. Oztek, Recovery of hydrogen and helium from their mixtures using metal hydrides, (2005).http://purl.fcla.edu/fcla/etd/CFE0000660
[3] J.R. Handley, W.C. Miller, Process requirements and enhanced economics of helium recovery from natural gas, in: SPE Mid-Continent Gas Symp., OnePetro, 1992.https://doi.org/10.2118/24292-MS
[4] C.A. Scholes, U.K. Gosh, M.T. Ho, The Economics of Helium Separation and Purification by Gas Separation Membranes, Ind. Eng. Chem. Res. 56 (2017) 5014–5020. https://doi.org/10.1021/acs.iecr.7b00976.
[5] J. Sunarso, S.S. Hashim, Y.S. Lin, S.M. Liu, Membranes for helium recovery: An overview on the context, materials and future directions, Sep. Purif. Technol. 176 (2017) 335–383.https://doi.org/10.1016/j.seppur.2016.12.020
[6] G.Q. Lu, J.C.D. Da Costa, M. Duke, S. Giessler, R. Socolow, R.H. Williams, T. Kreutz, Inorganic membranes for hydrogen production and purification: A critical review and perspective, J. Colloid Interface Sci. 314 (2007) 589–603.https://doi.org/10.1016/j.jcis.2007.05.067
[7] K. Kammermeyer, Technical gas permeation processes, Chemie Ing. Tech. 48 (1976) 672–675. https://doi.org/10.1002/cite.330480804
[8] K. Keizer, R.J.R. Uhlhorn, T.J. Burggraaf, Gas separation using inorganic membranes, in: Membr. Sci. Technol., Elsevier, 1995: pp. 553–588. https://doi.org/10.1016/S0927-5193(06)80014-8
[9] H. Meinema, R.W.J. Dirrix, H.W. Brinkman, R.A. Terpstra, J. Jekerle, P.H. Kösters, Ceramic membranes for gas separation- recent developments and state of the art, Interceram. 54 (2005) 86–91. https://www.betase.nl/downloads/Interceram-ceramic-membranes.pdf
[10] J.P. Collins, J.D. Way, Hydrogen-selective membrane, (1997). https://patentimages.storage.googleapis.com/50/9b/54/51c93184da81b5/US5652020.pdf
[11] J. Song, L. Li, X. Tan, K. Li, BaCe0. 85Tb0. 05Co0. 1O3− δ perovskite hollow fibre membranes for hydrogen/oxygen permeation, Int. J. Hydrogen Energy. 38 (2013) 7904–7912. https://doi.org/10.1016/j.ijhydene.2013.04.104
[12] S.M. Saufi, A.F. Ismail, Fabrication of carbon membranes for gas separation—a review, Carbon N. Y. 42 (2004) 241–259. https://doi.org/10.1016/j.carbon.2003.10.022
[13] A.J. Bird, D.L. Trimm, Carbon molecular sieves used in gas separation membranes, Carbon N. Y. 21 (1983) 177–180. https://doi.org/10.1016/0008-6223(83)90076-3
[14] C.W. Jones, W.J. Koros, Carbon molecular sieve gas separation membranes-I. Preparation and characterization based on polyimide precursors, Carbon N. Y. 32 (1994) 1419–1425. https://doi.org/10.1016/0008-6223(94)90135-X
[15] C.A. Scholes, U.K. Ghosh, Review of membranes for helium separation and purification, Membranes (Basel). 7 (2017) 9. https://doi.org/10.3390/membranes7010009
[16] C.A. Scholes, U. Ghosh, Helium separation through polymeric membranes: selectivity targets, J. Memb. Sci. 520 (2016) 221–230. https://doi.org/10.1016/j.memsci.2016.07.064
[17] S. Wei, S. Zhou, Z. Wu, M. Wang, Z. Wang, W. Guo, X. Lu, Mechanistic insights into porous graphene membranes for helium separation and hydrogen purification, Appl. Surf. Sci. 441 (2018) 631–638. https://doi.org/10.1016/j.apsusc.2018.02.111.
[18] R. Antunes, A. Böhmländer, A. Bükki-Deme, B. Krasch, M.M. Cruz, L. Frances, Experimental investigation of the ideal selectivity of MFI-ZSM-5 zeolite-type membranes for a first evaluation of the separation of hydrogen isotopologues from helium, Sep. Purif. Technol. 212 (2019) 767–773. https://doi.org/10.1016/j.seppur.2018.11.088
[19] R. Spillman, Economics of gas separation membrane processes, in: Membr. Sci. Technol., Elsevier, 1995: pp. 589–667. https://doi.org/10.1016/S0927-5193(06)80015-X
[20] Y. She, S.C. Emerson, N.J. Magdefrau, S.M. Opalka, C. Thibaud-Erkey, T.H. Vanderspurt, Hydrogen permeability of sulfur tolerant Pd–Cu alloy membranes, J. Memb. Sci. 452 (2014) 203–211. https://doi.org/10.1016/j.memsci.2013.09.025
[21] F.C. Gielens, R. Knibbeler, P. Duysinx, M. Vorstman, J. Keurentjes, T. Duy Hien, Influence of steam and carbon dioxide on the hydrogen flux through thin Pd/Ag and Pd membranes, J. Memb. Sci. 279 (2006) 176–185. https://doi.org/10.1016/j.memsci.2005.12.002.
[22] H. Yin, A.C.K. Yip, A review on the production and purification of biomass-derived hydrogen using emerging membrane technologies, Catalysts. 7 (2017) 297. https://doi.org/10.3390/catal7100297
[23] R. Parashar, B.C. Nailwal, N. Goswami, R.K. Lenka, S. Kar, A. Kumar, A.K. Sinha, S.C. Parida, S. Mukhopadhyay, Composite Palladium Alloy Membranes for Separation and Recovery of Hydrogen in Bio-jet Fuel Production Unit Graphical abstract Keywords, 8 (2022) 1–9. https://doi.org/10.22079/JMSR.2022.553098.1547.
[24] S. Liguori, K. Kian, N. Buggy, B.H. Anzelmo, J. Wilcox, Opportunities, and Challenges of Low-Carbon Hydrogen via Metallic Membranes, Prog. Energy Combust. Sci. 80 (2020) 100851. https://doi.org/10.1016/j.pecs.2020.100851.
[25] S. Uemiya, State-of-the-art of supported metal membranes for gas separation, Sep. Purif. Methods. 28 (1999) 51–85. https://doi.org/10.1080/03602549909351644
[26] V. Violante, Integrated membrane water shift reactor/separator for tritium recovery in the fusion fuel cycle, in: Fusion Technol. 1992, Elsevier, 1993: pp. 1240–1243. https://doi.org/10.1016/B978-0-444-89995-8.50242-3
[27] N.A. Al-Mufachi, N. V Rees, R. Steinberger-Wilkens, Hydrogen selective membranes: A review of palladium-based dense metal membranes, Renew. Sustain. Energy Rev. 47 (2015) 540–551. https://doi.org/10.1016/j.rser.2015.03.026
[28] D. Demange, S. Stämmler, M. Kind, A new combination of membranes and membrane reactors for improved tritium management in breeder blanket of fusion machines, Fusion Eng. Des. 86 (2011) 2312–2316. https://doi.org/10.1016/j.fusengdes.2010.12.083
[29] L.S. Mcleod, Hydrogen Permeation Through Microfabricated Palladium-Silver Alloy Membranes, Dr. Philos. Thesis. (2008) 164. https://smartech.gatech.edu/bitstream/handle/1853/31672/mcleod_logan_s_200812_phd.pdf?sequence=1
[30] S.C. Chen, G.C. Tu, C.C.Y. Hung, C.A. Huang, M.H. Rei, Preparation of palladium membrane by electroplating on AISI 316L porous stainless steel supports and its use for methanol steam reformer, J. Memb. Sci. 314 (2008) 5–14. https://doi.org/10.1016/j.memsci.2007.12.066
[31] S. Yun, S.T. Oyama, Correlations in palladium membranes for hydrogen separation: A review, J. Memb. Sci. 375 (2011) 28–45. https://doi.org/10.1016/j.memsci.2011.03.057
[32] N. Itoh, A membrane reactor using palladium, AIChE J. 33 (1987) 1576–1578. https://doi.org/10.1002/aic.690330921

[33] M. Incelli, A. Santucci, S. Tosti, M. Carlini, Design of a multi-tube Pd-membrane module for tritium recovery from He in DEMO, Processes. 4 (2016) 40.https://doi.org/10.3390/pr4040040
[34] S. Adhikari, S. Fernando, Hydrogen membrane separation techniques, Ind. Eng. Chem. Res. 45 (2006) 875–881. https://doi.org/10.1021/ie050644l.
[35] M. De Falco, L. Marrelli, G. Iaquaniello, Membrane reactors for hydrogen production processes, (2011).Springer London. DOI 10.1007/978-0-85729-151-6.
[36] M. Malo, I. Peñalva, J. Azkurreta, B. Garcinuño, H.D. Liu, D. Rapisarda, H.S. Zhou, G.N. Luo, Experimental Determination of Hydrogen Isotope Transport Parameters in Vanadium, Membranes (Basel). 12 (2022) 1–10. https://doi.org/10.3390/membranes12060579.
[37] G. Bellanger, Prospecting stress formed by hydrogen or isotope diffused in palladium alloy cathode, Materials (Basel). 11 (2018) 2101. https://doi.org/10.3390/ma11112101
[38] J.J. Conde, M. Maroño, J.M. Sánchez-Hervás, Pd-Based Membranes for Hydrogen Separation: Review of Alloying Elements and Their Influence on Membrane Properties, Sep. Purif. Rev. 46 (2017) 152–177. https://doi.org/10.1080/15422119.2016.1212379.
[39] R.E. Buxbaum, R. Subramanian, J.H. Park, D.L. Smith, Hydrogen transport and embrittlement for palladium coated vanadium—chromium—titanium alloys, J. Nucl. Mater. 233 (1996) 510–512. https://doi.org/10.1016/S0022-3115(96)00239-5
[40] A. Suzuki, H. Yukawa, T. Nambu, Y. Matsumoto, Y. Murata, Quantitative evaluation of hydrogen solubility and diffusivity of V–Fe alloys toward the design of hydrogen permeable membrane for low operative temperature, Mater. Trans. 57 (2016) 1823–1831. HTTP://doi.org/10.2320/matertrans.MAW201604
[41] Y. Fukai, Diffusion. In: The Metal-Hydrogen System (2005).Springer Series in Materials Science, vol 21. Springer, Berlin, Heidelberg. https://doi.org/10.1007/3-540-28883-X_6
[42] V.N. Alimov, A.O. Busnyuk, S.R. Kuzenov, E.U. Peredistov, A.I. Livshits, Bcc V–Fe alloys for the hydrogen separation membranes: Hydrogen solubility and global character of alloying effect, J. Memb. Sci. 644 (2022) 120159. https://doi.org/10.1016/j.memsci.2021.120159
[43] V.N. Alimov, I. V. Bobylev, A.O. Busnyuk, S.N. Kolgatin, S.R. Kuzenov, E.Y. Peredistov, A.I. Livshits, Extraction of ultrapure hydrogen with V-alloy membranes: From laboratory studies to practical applications, Int. J. Hydrogen Energy. 43 (2018) 13318–13327. https://doi.org/10.1016/j.ijhydene.2018.05.121.
[44] B.C. Nailwal, N. Goswami, R.K. Lenka, A.K. Singha, H.Z. Fani, A.S. Rao, A. Ghosh, R.C. Bindal, S. Mohan, S. Kar, Multi-tube tantalum membrane reactor for HIx processing section of IS thermochemical process, Int. J. Hydrogen Energy. 45 (2020) 24341–24354. https://doi.org/10.1016/j.ijhydene.2020.06.263
[45] S.W. Nam, S.P. Yoon, H.Y. Ha, S.-A. Hong, A.P. Maganyuk, Methane steam reforming in a Pd-Ru membrane reactor, Korean J. Chem. Eng. 17 (2000) 288–291. https://doi.org/10.1007/BF02699042
[46] F.C. Gielens, H.D. Tong, M.A.G. Vorstman, J.T.F. Keurentjes, Measurement and modeling of hydrogen transport through high-flux Pd membranes, J. Membr. Sci. 289 (2007) 15–25. https://doi.org/10.1016/j.memsci.2006.11.029

Supplementary Information

S.1 Fabrication of composite alumina support tubes

A slurry of alumina and clay was prepared followed by extrusion to obtain green clay-alumina tubes. The composition of the clay-alumina support tube was 92% alumina and 8% clay (47% SiO_2, 38% Al_2O_3, rest Fe_2O_3, TiO_2, and low ignition compounds). A 6% aqueous solution of polyvinyl alcohol (PVA) was prepared and a 1.5% solution of PVA per kg of the solid mixture was used for the extrusion of the tubes. The sintering profile adapted is given in Table S1. The final temperature for sintering was varied from 1300 to 1500 ˚C at an incremental value of 100 ˚C. A low heating rate was maintained to avoid crack generation in the tube. A constant temperature at 300 ˚C is maintained for 1 h to provide enough time for the burning of binder (PVA).

Characterization of base support was carried out using a mercury porosimeter (PASCAL - 440). To reduce the pore size of ceramic support, an intermediate layer of alumina was developed over a clay-alumina support tube. Alumina (particle size: 190 nm) coating of base clay-alumina support tubes was done by a dip coating method. Alumina slurry (10% solid loading) in methyl ethyl ketone (50%) and ethanol (50%) was prepared with polyvinyl butyryl (PVB) as binder (4%), oleic acid (3% of alumina) as dispersant and dioctyl phthalate (DOP) (13% of alumina) and polyethylene glycol (PEG) of molecular weight 400 kDa (13% of alumina) as a plasticizer. The slurry was coated on alpha alumina. All the alumina-coated tubes were sintered at 700 ˚C, with heating rates of 1 ˚C/min till 300 ˚C (constant heating for 1 h), followed by a rate of 3 ˚C/min till 700 ˚C, and cooling up to RT at a rate of 3 ˚C/min.

Table S1

Sintering profile adapted for sintering of clay-alumina tubes.

Segment	Ramp/Dwell	Initial temperature (˚C)	Final temperature(˚C)	Heating rate (˚C/ min)	Duration (h)
1	Heating rate	RT	300	1	-
2	Constant temperature heating	300	300	-	1
3	Heating rate	300	1600	3	-
4	Constant temperature heating	1600	1600	-	3
5	Cooling rate	1600	RT	3	-

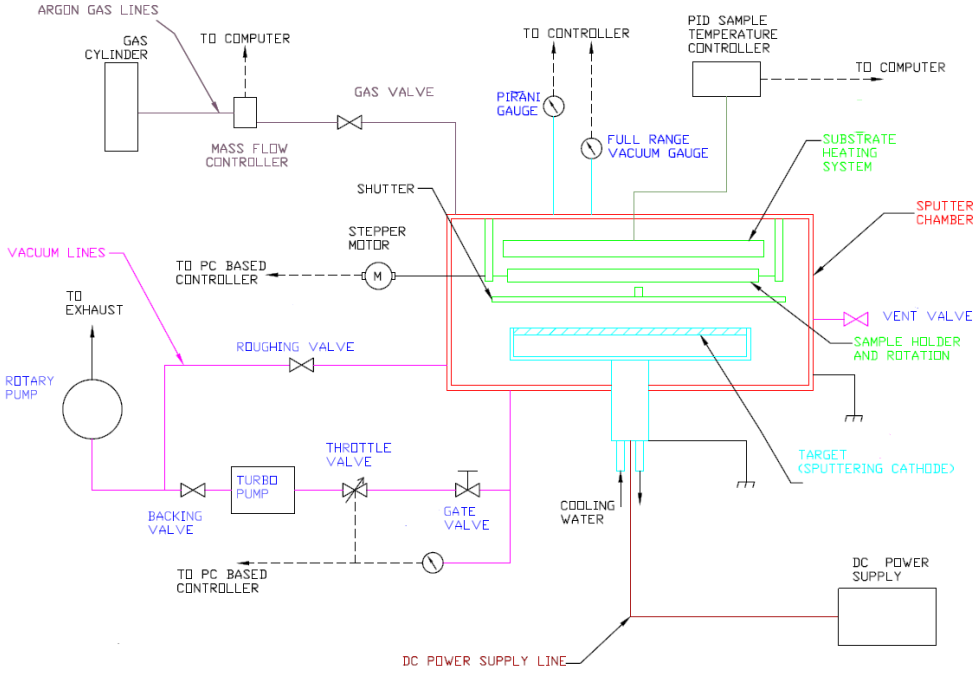

Fig. S1. Schematic of the DC magnetron sputtering unit.

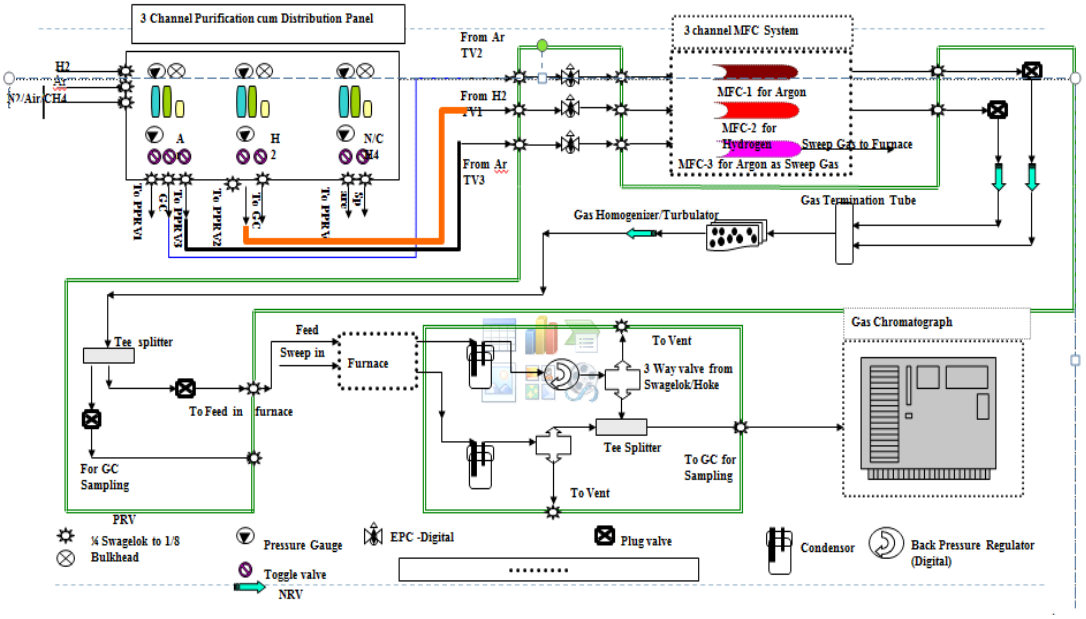

Fig. S2. Gas permeation setup.

Fig. S3. In-house synthesized composite alumina tubes.

Fig. S4. In-house synthesized composite V-Fe membrane.

S.2 Computational Approach

S.2.1 Governing equations

Momentum Transport:

The flow is laminar with a typical Reynolds number of the order of 1. Thus, to model momentum transport, Navier-Stokes equation as given by Equation 1 and 2 are used.

$$\rho \boldsymbol{u}.\nabla \boldsymbol{u} = \nabla.\left[-p\boldsymbol{I} + \eta(\nabla \boldsymbol{u} + \nabla \boldsymbol{u}^T) - \left(\frac{2\eta}{3}\right)(\nabla.\boldsymbol{u})\boldsymbol{I}\right] \quad (1)$$

$$\nabla.(\rho \boldsymbol{u}) = 0 \quad (2)$$

Where, ρ denotes the density of the gaseous mixture in kg/m^3, u represents the velocity vector of the gaseous mixture in m/s, η denotes the viscosity of the gaseous mixture in Pa.s, and p represents the pressure of the gaseous mixture in Pa.

Energy Transport:

Equation 3 gives the energy transport equation used in the modeling. The equation accounts for both convective and conductive transport of the heat.

$$\rho C_p(\boldsymbol{u}.\nabla T) = \nabla.(k_t \nabla T) \quad (3)$$

Where T is the temperature of the gaseous mixture (K), C_p is the specific heat at a constant pressure of the gaseous mixture (J/mol.K), and k_t is the effective thermal conductivity of the gaseous mixture (W/m.K).

Species Transport:

The species transport equation for individual components (H_2 and He) is the steady state Maxwell-Stefan diffusion and convection equation as given by Equation 4.

$$\nabla.\left(\rho\omega_i \boldsymbol{u} - \rho\omega_i \sum_{j=1}^{n} D_{ij}\left(\nabla x_j + \left(x_j - \omega_j\right)\frac{\nabla p}{p}\right)\right) = 0 \quad (4)$$

In the above equation, ω_i is the mass fraction of species i, x_j is the molar fraction of species j and D_{ij} is the ij component of the multi-component diffusivity. The equation is solved only for one component (H_2), and for the second component (He) mass fraction constraint equation is used.

S.2.2 Physical properties used in transport equations

The effective molecular weight and density of the gaseous mixture are calculated using the following equations:

$$M_{mix} = \sum(x_i \times M_i) \quad (5)$$

$\rho = M_{mix} \times (p/RT)$ (6)

In the above equation, M_i molecular mass of component i (g/mol) (i = 1, 2 for He and H_2 respectively) M_{mix} molecular mass of gas mixture (g/mol), the x_i mole fraction of component i (i= 1 (He), 2 (H_2)), ρ effective density of gas mixture (kg/m^3), R is the universal gas constant (J/mol.K), p is pressure (Pa), T is temperature of gaseous mixture (K).

The effective thermal conductivity of the gas mixture is calculated using the equation formulated by Lindsay et al. [1] and Buddenberg et al. [2]:

$$k_t = \sum_{i=1}^{n} \frac{k_i}{1+\frac{1}{x_i}\sum_{j=1}^{n} A_{ij}x_j} \quad (7)$$

A_{ij} in Equation 7 is calculated by Equation 8:

$$A_{ij} = \frac{1.385\,\mu_i}{Dij\rho_i} \quad (8)$$

Where μ_i is the viscosity of component i (kg/m.s).

The specific heat of the species as well as the effective heat capacity of the gas mixture is calculated by the following equations:

$C_{pH2} =$ 6.62 +0.00081T (J.mol^{-1}.K^{-1}) (9)

$C_{pHe} =$ 20.772 (J.mol^{-1}.K^{-1}) (10)

$$C_p = \sum x_i \times C_{pi} \quad (11)$$

The effective viscosity is defined by the following equation as given by Buddenburg et al. [2]:

$$\eta = \frac{\eta_1}{1+(\frac{1.385\eta_1}{x_1\rho_1})\times(\frac{x_2}{D_{12}})} + \frac{\eta_2}{1+(\frac{1.385\eta_2}{x_2\rho_2})\times(\frac{x_1}{D_{12}})} \quad (12)$$

The viscosity of each component in the gas mixture depends on the temperature according to the following equation:

$\eta_i = \eta_0 * (T/T_s)^n$ (13)

Where, n = 0.680 for helium and 0.646 for hydrogen.

For H_2, T_s = 273K and η_0 = 1.85 x 10^{-5} Pa.s.

For He, T_s = 285K and η_0 = 8.399 x 10^{-6} Pa.s.

The diffusivity of hydrogen in helium is taken as 5 x 10^{-4} m^2/s [3].

Assumptions in the model:

The assumptions considered in the CFD model are as follows:

- The system is in a steady state.
- All the mass transfer resistance is due to the metal coating.
- Simulations were carried out for the feed side (annular region) only.
- The gaseous mixture is assumed to show ideal gas behavior. Thus, density changes occur due to heat transfer and due to the permeation of hydrogen only.
- Flow is considered to be laminar (Reynolds number of the order of 1).

Fig. S5 shows the computational domain used for simulating the metal membrane permeator. The computational domain is taken to be two-dimensional axisymmetric. For initial simulation studies (for single tube), the length of the membrane is taken to be 250 mm and the inner diameter of the domain (diameter of membrane tube) and the outer diameter of the domain (diameter of housing) is taken to be 10 and 14.14 mm, respectively. The feed flows in the annular space.

S.2.3 Boundary conditions

Boundary conditions for momentum transport:

For momentum transport, the Navier-Stokes equation is solved, in which the following boundary conditions have been defined:

At inlet: $\boldsymbol{u_z} =$ u_0 (velocity boundary condition).

At outlet: p = P (pressure boundary condition).

Boundary conditions for energy transport:

For energy transport, the following boundary conditions have been defined:

At the membrane and housing surface: T_w = 700 K (constant temperature boundary condition).

At inlet: $T = T_f$.

At the outlet: $k_t \nabla T = 0$ (Convective flux boundary condition). (14)

Boundary conditions for species transport:

For species transport, the following boundary conditions have been defined:

At the membrane wall, hydrogen permeation flux is given by Equation 15:

$H_f = -Pe \times p \times x_{H2} \times M_{H2}$ (15)

Where H_f is the permeation flux of hydrogen in kg/m^2.s, *Pe* is the hydrogen permeance in mol.m^{-2}.h^{-1}Pa and the partial pressure of hydrogen in Pa, M_{H2} is the molecular mass of hydrogen, and x_{H2} is the mole fraction of hydrogen.

At the membrane wall, the permeation flux of hydrogen is the product of the hydrogen permeability of the membrane and the partial pressure of hydrogen at a given location along the membrane wall. The permeation flux of helium (He_f) is considered zero, as the metal membrane permeates only hydrogen.

At the wall of housing: H_f, He_f= 0.

At the inlet: Mole fraction of hydrogen = x_{H2} (mole fraction condition).

At the outlet: (16)

$\left(-\rho\omega_i \sum_{j=1}^{n} D_{ij} \left(\nabla x_j + \left(x_j - \omega_j\right)\frac{\nabla p}{p}\right)\right) = 0$ (Convective flux boundary condition).

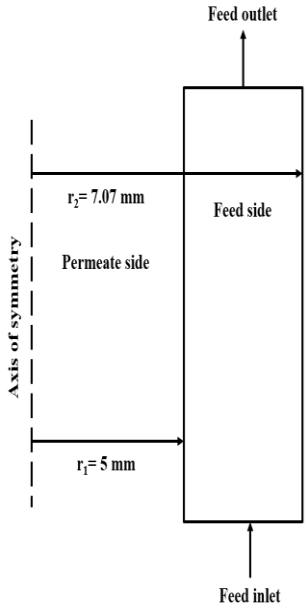

Fig. S5. Computational domain used for simulation of V-Fe metal membrane permeator.

S.2.4 Grid Independence Test

One of the objectives of the preliminary simulations was to carry out a grid independence test. For this simulation were carried out using different grid sizes or densities to find out the grid density beyond which results become grid-independent. Fig. S6 shows the five different grids used to carry out grid independence tests. These grids have been called coarser, coarse, normal, fine and finer. The conditions used for these simulations are: feed velocity, u_0 = 0.01 m/s, feed temperature, T_f= 600 K, wall temperature, T_w= 700 K, pressure at the outlet, P = 1 atm. The feed gas mixture contains 90% (mole percentage) H_2.

The results for the grid independence tests are shown in Fig. S7 (a) and (b) for both single-tube and scaled-up systems. The tracked parameter is the mole fraction of hydrogen at the exit of the reactor. With the reduction in grid size (increasing grid density), the mole fraction of hydrogen at the outlet first increases, and then becomes constant. There is an insignificant change in the mole fraction of hydrogen at the outlet of the membrane beyond the fine mesh. Thus, fine mesh is considered the optimum mesh for further simulations for both systems (single tube and scaled-up).

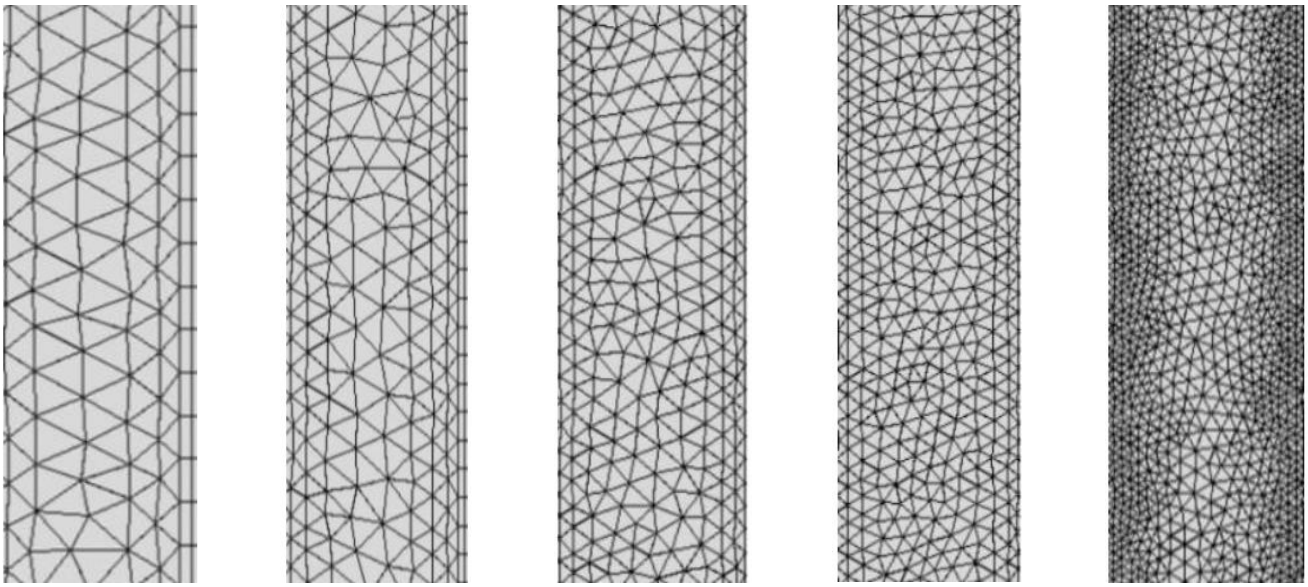

Coarser (647 elements/cm^2) | Coarse (1640 elements/cm^2) | Normal (2569 elements/cm^2) | Fine (4355 elements/cm^2) | Finer (11547 elements/cm^2)

Fig. S6. Different grids used for grid independence test.

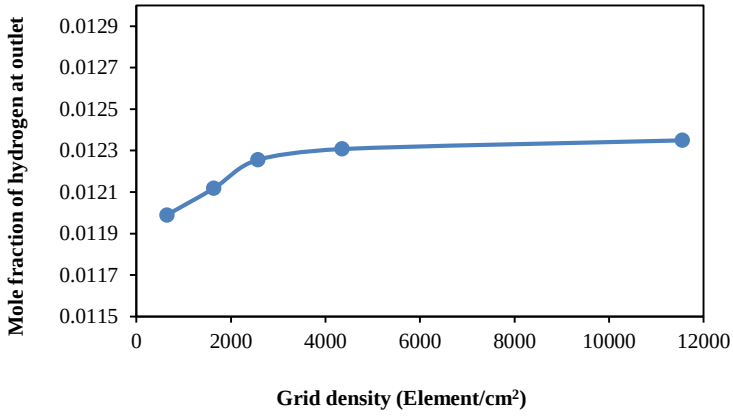

(a) Single tube system

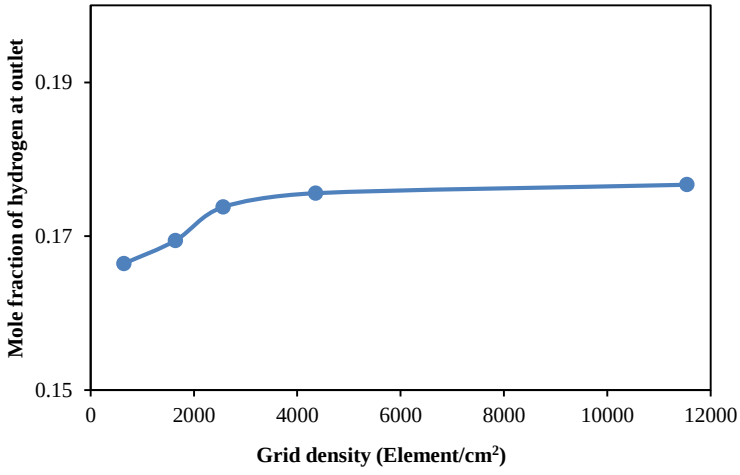

(b) Scaled-up system.

Fig. S7. Mole fraction of hydrogen at the outlet for different grid densities (a) for single tube (b) for the scaled-up system.

S.2.5 Validation and preliminary simulations

The CFD model was validated by comparing the velocity profile predicted by the model for the case of zero hydrogen flux with the analytical velocity profile. In this case, the analytical the velocity profile is the velocity profile for laminar flow in an annulus. The analytical velocity profile is given by Equation 17 by R.B. Bird [4]. Fig. S8 gives the comparison of the predicted and the analytical velocity profile. A very good agreement between the two profiles can be observed.

$$V = \frac{(P_o - P_L)\,R^2}{(4\mu L)}\left[1 - \left(\frac{r}{R}\right)^2 - \frac{1-k^2}{\ln\left(\frac{1}{k}\right)} \times \ln\left(\frac{R}{r}\right)\right] \quad (17)$$

$$V_{max} = \frac{(P_o - P_L)R^2}{4\mu L}\left[1 - \wedge^2(1 - ln\gamma^2)\right] \quad (18)$$

$$\text{Where, } \gamma^2 = \frac{(1-(k)^2}{2\ln(1/k)} \;\&\; k = \left(\frac{r}{R}\right) \quad (19)$$

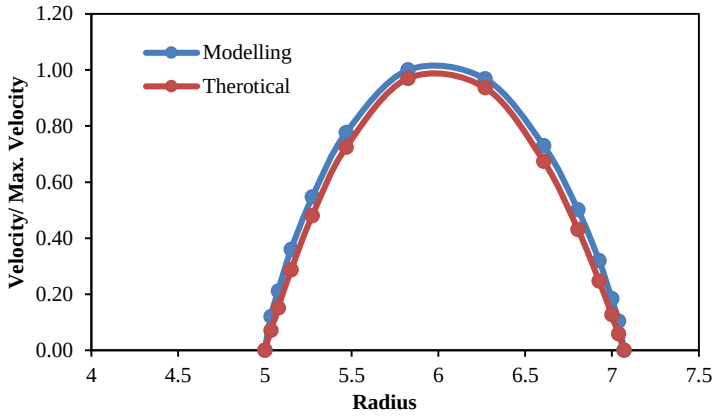

Fig. S8. Comparison between the modeling and analytical solutions of a velocity profile for annular flow (T_f= 600K, T_w = 700K, P = 1 bar, u_0 =0.01 m/s, x_{H2}= 0.9).

REFERENCES

[1] Katz JL, Cohen ER, Thermal conductivity of gas mixtures, 8 (1970) 15–18. https://doi.org/10.1021/ie50488a017.

[2] J.W. Buddenberg, C.R. Wilke, Calculation of gas mixture viscosities., Ind. Eng. Chem. 41 (1949) 1345–1347. https://doi.org/10.1021/ie50475a011

[3] H.K. Chung, A. Dalgarno, Diffusion of hydrogen atoms in helium gas and helium atoms in hydrogen gas, Phys. Rev. A. 66 (2002) 12712. https://doi.org/10.1103/PhysRevA.66.012712

[4] R.B. Bird, W.E. Stewart, E.N. Ligtfoot, Transport phenomena, 2nd Ed. (2002). https://doi.org/10.1115/1.1424298